

Fusing Monocular RGB Images with AIS Data to Create a 6D Pose Estimation Dataset for Marine Vessels

Fabian Holst*,¹ , Emre Gülsoylu*,¹ , Simone Frintrop¹ 

Abstract—The paper presents a novel technique for creating a 6D pose estimation dataset for marine vessels by fusing monocular RGB images with Automatic Identification System (AIS) data. The proposed technique addresses the limitations of relying purely on AIS for location information, caused by issues like equipment reliability, data manipulation, and transmission delays. By combining vessel detections from monocular RGB images, obtained using an object detection network (YOLOX-X), with AIS messages, the technique generates 3D bounding boxes that represent the vessels’ 6D poses, i.e. spatial and rotational dimensions. The paper evaluates different object detection models to locate vessels in image space. We also compare two transformation methods (homography and Perspective-n-Point) for aligning AIS data with image coordinates. The results of our work demonstrate that the Perspective-n-Point (PnP) method achieves a significantly lower projection error compared to homography-based approaches used before, and the YOLOX-X model achieves a mean Average Precision (mAP) of 0.80 at an Intersection over Union (IoU) threshold of 0.5 for relevant vessel classes. We show indication that our approach allows the creation of a 6D pose estimation dataset without needing manual annotation. Additionally, we introduce the Boats on Nordelbe Kehr wieder (BONK-pose), a publicly available dataset comprising 3753 images with 3D bounding box annotations for pose estimation, created by our data fusion approach. This dataset can be used for training and evaluating 6D pose estimation networks. In addition we introduce a set of 1000 images with 2D bounding box annotations for ship detection from the same scene.

Index Terms—6D Pose Estimation, Automated Identification System, Ship Detection, Data Fusion.

I. INTRODUCTION

The Automatic Identification System (AIS) aids in collision avoidance and enhances situational awareness for vessels and waterway management authorities [1] by providing information on vessels’ position, course, and speed among other fields. Relying purely on AIS data for localisation has limitations, induced by equipment reliability issues [2], [3], manipulation [4], and delayed transmission that can lead to position drift.

To overcome the limitations of relying only on AIS, researchers have explored associating vessel instances (bounding boxes) with their respective AIS messages [5]–[11]. By integrating visual information from monocular RGB images with AIS data, these approaches improve identification and tracking of vessels [12], particularly in challenging environments where AIS signals may be incomplete, noisy, or subject to malicious modification. Despite these advancements, a critical challenge remains open: the accurate estimation of a vessel’s six degrees of freedom (6D) pose, that is, determining both its three spatial

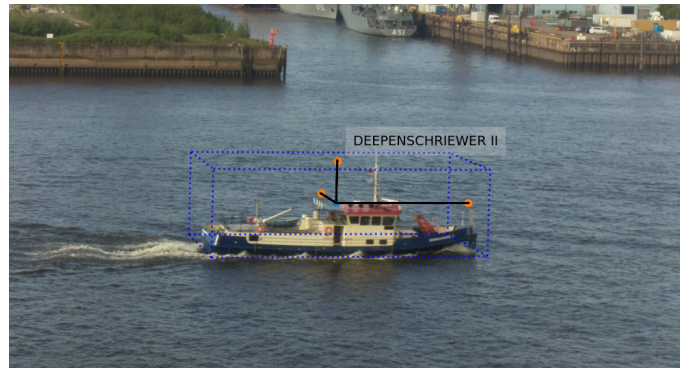


Fig. 1: A sample visualisation of a 6D pose annotation, automatically created by fusion of AIS data and a predicted 2D bounding box. The 3D bounding box (blue dotted lines) encompasses the vessel and is aligned with the vessel’s dimensions. The black axes with orange dots at the end represents the vessel’s coordinate axes.

(position) and three rotational (orientation) dimensions. This information can be inferred through AIS data and monocular RGB image fusion, as demonstrated by this paper. Achieving accurate 6D pose estimation is challenging due to factors like occlusions, sensor noise, varying lighting conditions, and scene clutter, especially in dynamic environments [13].

These challenges are not unique to the maritime field and the problem of 6D pose estimation has been extensively studied in other domains such as robotics [13], [14] and autonomous vehicles [15]. Similar to the challenges faced in autonomous car navigation, the accurate localisation and tracking of vessels in maritime environments is a critical task for ensuring safety and efficiency in waterway management [16]. Leveraging 6D pose estimation, vessels can be represented as 3D bounding boxes, allowing for the estimation of their full spatial dimensions. This can complement the missing dimension information in AIS, which does not include the air draught information. Implementing 6D pose estimation would enrich the data for better localisation of vessels for waterway management and enable the detection of dimension-related disparities for surveillance.

While systems like Light Detection and Ranging (LiDAR) or Radio Detection and Ranging (RADAR) offer point clouds on which the 6D pose of a vessel can be estimated [17], they are more expensive or have restricted ranges compared to cameras [18] and are more suitable for berthing assistance systems [19]. Predicting the 6D pose of a vessel by using an RGB camera is important, as it would assist collision avoidance for autonomous ships and provides insights into vessel activities for traffic service and surveillance, while being much simpler and cheaper than LiDAR or RADAR.

¹University of Hamburg, Faculty of Mathematics, Informatics and Natural Sciences, Department of Informatics, Computer Vision Group, 22527, Hamburg, Germany. .

* denotes equal contribution

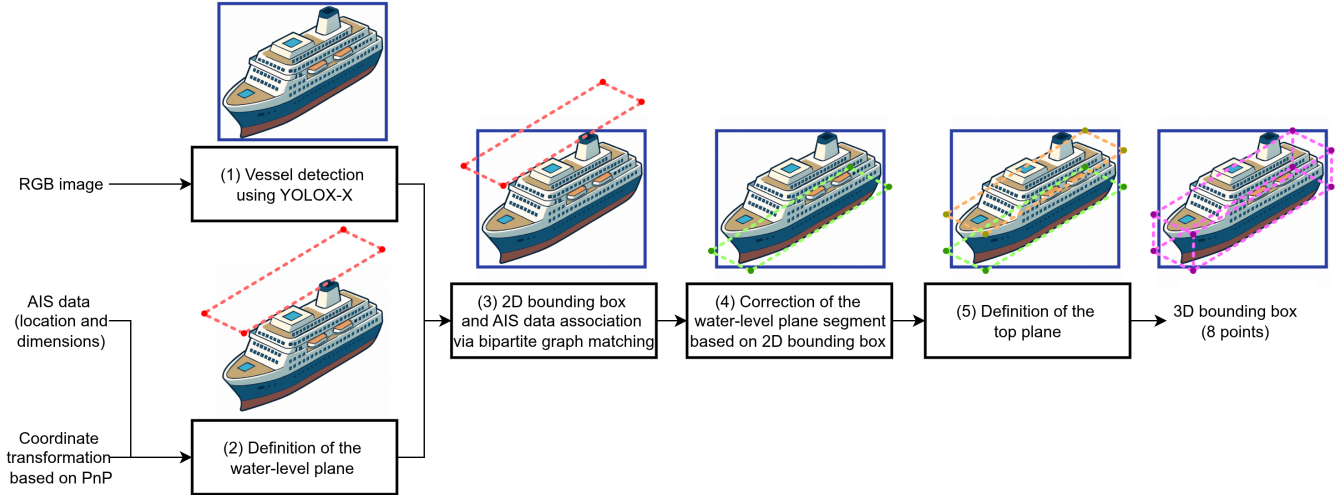


Fig. 2: Flowchart of the proposed technique for creating 3D bounding boxes from AIS data and RGB image fusion. The inputs are the RGB image, AIS data, and the coordinate transformation matrix obtained via the PnP algorithm: (1) Vessel detection using YOLOX-X and coordinate transformation of AIS data into image space based on the PnP algorithm. (2) Definition of the water-level plane segment using the vessel's location and dimensions. (3) Association of 2D bounding boxes and AIS data through bipartite graph matching. (4) Correction of the water-level plane segment position based on the associated 2D bounding box. (5) Translation of the water-level plane segment to create the top edge of the 2D bounding box, resulting in a 3D bounding box for the detected vessel.

So far there are no 6D pose estimation datasets specific to the maritime domain. In this work, we are addressing this gap by proposing a technique to create 3D bounding boxes using AIS data and monocular RGB images. Our technique involves detecting vessels in images using an object detection network, while simultaneously acquiring AIS messages. These detections are then associated with the AIS messages via bipartite graph matching. Finally, a 3D bounding box is created by fusing the two data sources as visualised in Fig. 1. The overview of the proposed technique is shown in Fig. 2. We evaluate the effectiveness of various "off-the-shelf" object detection models and compare different transformation methods between image and world space. These methods are homography, as it is frequently used in the literature, and Perspective n-point (PnP) [20], which has not been used for this task before. We also assess the performance of our AIS matching algorithm and 3D bounding box creation algorithm.

Using the proposed technique, we created a novel and publicly available 6D pose estimation dataset, Boats on Nordelbe Kehrwieler (BONK-Pose), comprising 3753 annotated images. This dataset consists of RGB images taken by the River Elbe, relevant AIS messages, and annotations for training 6D pose estimation or ship detection networks. A sample image with annotations is shown in Fig. 1.

Our goal is to allow machine learning based 6D pose estimation in the maritime domain, by both providing a dataset with ground truth and introducing a method to create further such datasets in a way that is not bottlenecked by manual annotation work.

We can summarise our contributions as follows:

- A novel, automated technique for generating a 6D pose estimation dataset for marine vessels,

- A new and publicly available dataset¹, Boats on Nordelbe Kehrwieler (BONK-Pose), for ship detection and 6D pose estimation,
- Detailed evaluation of the proposed technique.

II. RELATED WORK

There are already numerous studies focused on the fusion of RGB images with AIS data. This fusion requires not only detecting vessels in images but also accurately associating each detected vessel with its transmitted AIS messages based on spatial and temporal information.

Lu et al. [7] addressed this by using a modified YOLOv5 [21] model to detect vessels in images from a shore-based camera overlooking the English Channel. By employing Dead Reckoning (DR) to predict vessel positions at the image time and matching based on distance and bearing thresholds, they associated 72% of message-vessel pairs. Limitations were due to inaccuracies in object detection and distance estimation, especially when vessel orientations did not match the assumptions made in the approach.

Huang et al. [22] combined AIS data with vessel tracking in inland waterways. They used DeepSORT [23] for tracking, with daytime objects detected by a custom SSD-based model and nighttime objects by detecting onboard lighting. AIS positions were interpolated using DR. They applied homography to map image coordinates to real-world coordinates, enabling spatial distance calculations for matching.

Carrillo-Pérez et al. [10] employed similar techniques but used pixel-wise segmentations and transformed image coordinates to world coordinates via homography. They also introduced a novel dataset called ShipSG, designed for the

¹<https://fabianholst.github.io/BONK-pose/>

segmentation and georeferencing of ships in maritime monitoring scenes captured from static oblique views.

Extending [10] for panning cameras, Gülsoylu et al. [11] aimed to enrich basic object detection outputs with detailed AIS information like vessel type and course. They fine-tuned YOLOv5 to detect vessels in images from public webcams. By estimating a homography between image and world spaces, they associated detected ships with AIS messages.

While current research offers a strong base for detecting and associating vessels, there is still a significant gap in the current research. None of the existing works have fused AIS data with RGB images to create a full 3D bounding box. This is mainly because AIS data does not include height information, requiring additional processing and new techniques to determine ship heights. Addressing this challenge could benefit from examining advancements in other fields.

Similar to the maritime domain, detecting objects such as cars and people and estimating their 3D positions are crucial for decision making in autonomous driving [24]. Additionally, when estimating the pose of objects such as humans or cars in traffic, the rotational axes are constrained in a manner similar to that of vessels in water [25]. These similarities create a potential for applying methods between domains. For example, Mousavian et al. [26] address 6D pose estimation by first detecting 2D bounding boxes and estimating object dimensions based on category statistics. Combining these dimensions with rotation estimates allows them to project accurate 3D bounding boxes into image space, refining object positions within detections.

In the maritime domain, Kiefer et al. [25] focus on estimating the yaw of vessels while assuming minimal roll and pitch. They enhance the HyperPosePDF method [27], which uses a hypernetwork to generate probability distributions over possible rotations based on input images. By incorporating temporal information from multiple video frames, they improve accuracy by averaging out errors over time, resulting in more stable and precise yaw estimations.

Autonomous driving has several domain specific datasets for 6D pose estimation. KITTI [15] is an early and frequently used dataset. It provides LiDAR point clouds in addition to stereo images and a multitude of other sensor data. Another dataset is ApolloCar3D [28], which contains 5,277 images with over 60,000 instances of cars registered with their 3D CAD models. The 3D models are aligned with images by selecting keypoint matches between the models and visible parts of the vehicles. Annotations include the pose of each car in terms of translation and rotation relative to the camera.

Despite these advancements in autonomous driving, there remains a notable gap in the maritime domain. There are datasets available for tasks such as ship detection, including general purpose datasets like MS COCO [29] with their "boat" class or more tailored datasets to the maritime domain [30], as well as for instance segmentation [10], and ship tracking [31]. However, there are few works focused on 6D pose estimation for ships [25], [32], and none that leverage AIS data. This gap will be filled by our work.

III. METHODOLOGY

We propose a technique to create 3D bounding boxes by fusing AIS data with 2D bounding boxes. The proposed technique consist of five stages, as shown in Fig. 2: (1) The vessels in the image are detected by YOLOX-X [33] and the location information gathered from AIS data is transformed from world coordinates into image coordinates. This transformation is achieved through a camera model whose parameters are determined by the PnP algorithm. (2) The output of these operations, 2D bounding box predictions and available AIS data, are associated by bipartite graph matching. (3) Four points that encloses the vessel from bird's eye view are derived based on dimension information gathered from the AIS messages. These are obtained based on location, heading and vessel dimensions from AIS transformed into image space. The plane segment formed by these four corners is referred to as the water-level plane segment, which forms the bottom plane segment of the 3D bounding box. (4) As AIS is not completely accurate, as discussed in the Section I, this plane segment may not perfectly fit the actual pose of the vessel. Thus the 2D bounding box predicted by YOLOX-X serves as a guide to correct the position of the water-level plane segment. (5) The top plane segment of the 3D bounding box is created by translating the water-level plane segment upwards, using the top edge of the 2D bounding box as a restraint. The result of this technique is a 3D bounding box defined by 8 points for the detected vessel.

A. Vessel Detection

Many object detection models can be effectively applied to vessel detection using their "off-the-shelf" weights, thanks to datasets like MS COCO [29], which includes a *boat* class. In this context, we denote the output of the model as BB_{pred} , which corresponds to the predicted vessel locations in image space. To demonstrate that our technique does not rely on specialised models, we conducted experiments (see Section V-A) using generalised models.

For vessel detection, we selected YOLOX-X [33], a variant of the You Only Look Once (YOLO) family [34], which builds upon the YOLOv3 architecture [35]. The YOLOX model family offers several sizes: YOLOX-X, YOLOX-L, YOLOX-M, and YOLOX-S, which differ primarily in model complexity, size, and computational requirements. The smaller YOLOX-S and YOLOX-M variants are optimised for scenarios with limited computational resources, providing faster inference at the expense of some accuracy. In contrast, the larger YOLOX-L and YOLOX-X models deliver higher accuracy but require more computational power and have longer inference times.

YOLO models are widely recognised for their real-time object detection capabilities, thanks to their efficient single-stage detection approach that balances speed and accuracy [36]. Our goal is to establish a well-balanced baseline solution that can be further extended in future work.

B. Coordinate Transformation

Transforming world coordinates to image coordinates is required to align the georeferenced AIS data with object detec-

tions in image space. For this, we will compare homography based approach as used in related work [8], [10], [11], and a full pinhole camera model, whose parameters are estimated with PnP. Both of these methods require a set of keypoints where the coordinates are known in both image space and in real world coordinate system.

1) *Keypoint Selection*: We manually identified and annotated a set of points that are easily recognisable both in the real world and in the image. These points include distinct features such as the corners of buildings. For each of these points, we recorded their real-world coordinates and their corresponding coordinates in the image.

Homography assumes that all keypoints points lie on the same plane, making it useful for applications such as image stitching [37]. For our case, we can consider the water surface as a planar surface. However, defining keypoints is challenging due to the difficulty in distinguishing points on the water surface. Selecting keypoints on land is easier, but land surfaces are not coplanar with the water surface. Even without considering tidal effects, it is challenging to select keypoints where water intersects with a distinct artificial structure, such as a pier. We defined our points using artificially built structures, not all of these points are coplanar with the water surface.

To make our corresponding points suitable for homography, we used two approaches to make our real world keypoints coplanar on an interim plane. In one, we determined the tangential plane that touches the water surface that has the normal of the earth's surface at this point. In another approach, we applied Principle Component Analysis (PCA) on our set of 3D world corresponding points. PCA finds the axes along which the variance of the set is represented strongest. This allows us to choose the two axes that represent our 3D points in the best way possible, meaning losing the least information by excluding the least important principal component. With both approaches, we can arrive at two vectors in our 3D world space, that span an interim plane onto which we can project our corresponding points.

2) *Homography*: Homography is a technique that enables the transformation of coordinates from one plane to another using a homography matrix [38].

\mathbf{A} is the matrix with which we project our 3D points onto the interim plane. It is defined as

$$\mathbf{A} = [\mathbf{v}_1 \quad \mathbf{v}_2], \quad (1)$$

where \mathbf{v}_1 and \mathbf{v}_2 are 3D vectors, either two orthogonal vectors of the tangential plane, or the two most important principal components.

We project our 3D keypoints \mathbf{k}_{3d} onto the plane, calling them k_{2d} using the following transformation:

$$\mathbf{k}_{2d} = \mathbf{A}^T \mathbf{k}_{3d}. \quad (2)$$

The Homography matrix, \mathbf{H} , can be approximated by minimising the reprojection error when mapping the real world coordinates on the interim plane to known image coordinates. Once \mathbf{H} is obtained, we can transform real world coordinates into the image.

If $\mathbf{x}_1 = (u, v, 1)$ is a pixel location and $\mathbf{x}_2 = (x, y, 1)$ is a coordinate in our interim plane in the real world, we can transform between world and image by finding \mathbf{H} in

$$\mathbf{x}_1 = \mathbf{H}\mathbf{x}_2. \quad (3)$$

This mapping with a homography matrix between two planes skips the camera projection, avoiding the need to determine the camera's intrinsic and extrinsic matrix.

3) *Perspective-n-Point*: The Perspective n-point (PnP) algorithm is useful for estimating the pose (position and orientation) of a camera given a set of 3D points in world coordinates and their corresponding 2D projections in an image [39]. This method requires a more complex model of the relationship between real-world and image space, compared to homography. Here, we do not have to project our keypoints onto a interim plane in the real world, we can directly use the points spanning all three dimensions. We used a pinhole camera model [40] defined as follows:

$$\bar{\mathbf{x}} = \mathbf{K} \mathbf{\Pi} {}^c\mathbf{T}_w {}^w\mathbf{X}. \quad (4)$$

A point, ${}^w\mathbf{X}$, in the real world is first projected into a frame of reference relative to the camera, using the extrinsic parameters of the camera, ${}^c\mathbf{T}_w$. This matrix contains the 3D position ${}^c\mathbf{t}_w$ of the camera, as well as its rotation in the world ${}^c\mathbf{R}_w$. $\mathbf{\Pi}$ is the projection matrix of a perspective projection, reducing the dimensionality by projecting onto a plane, as is the intrinsic camera matrix containing its field of view, aspect ratio, etc. The result is an image space coordinate $\bar{\mathbf{x}}$ [41].

The camera's intrinsic matrix \mathbf{K} is approximated for the specific camera model using chequerboard calibration. Given \mathbf{K} and a set of n point correspondences in 2D to 3D, the extrinsic matrix ${}^c\mathbf{T}_w$ is approximated with PnP.

With the established capability to perform transformations between world coordinates and image space, we can now project AIS-based data, such as vessel's location, onto the corresponding image.

C. Defining water-level plane segment

The water-level plane segment is defined by four 3D corner points on the water surface in world coordinates, and serves as the geometric base for constructing the full 3D bounding box for 6D pose estimation.

1) *Data in AIS*: AIS data is transmitted as a collection of standardised message types. The most relevant for vessel localisation and tracking are Position Reports, which carry dynamic information like position, speed, and course. Furthermore there are Static and Voyage Related Data messages, including vessel identity, type, dimensions, and voyage details.

AIS emitters are categorised based on the class of the transceiver: Class A and Class B [42]. Class A devices are mandatory for larger commercial vessels and transmit at higher power and more frequent intervals, providing more detailed navigational data. In contrast, Class B devices are designed for smaller vessels, transmit less frequently, and at lower power, carrying a reduced set of data fields compared to Class A.

In our work, we focussed on Class A AIS messages. By collecting these types of AIS messages, we can aggregate them by vessel identity to create a initial pose per vessel.



Fig. 3: AIS-based vessel location, \mathbf{a}_{3d} (orange) and water-level plane segment corners c_{3d} (blue). Dead reckoning vector, \mathbf{dr} (red) and corrected water-level plane segment corners c_{3d} (green) after dead reckoning. The older position in AIS does not match up with the image, dead reckoning improves this, but the inaccuracy of the AIS pose still leaves a small mismatch.

2) Using data from AIS to create a initial 6D pose:

The location data transmitted in AIS by the vessels is obtained via Global Positioning System (GPS). GPS data is based on EPSG:4979 [43], a geographic coordinate system that represents locations on the Earth's surface with angles (*longitude* and *latitude*) on a spherical Earth model. This type of representation is not fitting for the 6D pose estimation problem. Therefore, we converted the geographic coordinate (EPSG:4979) into a geocentric coordinate system EPSG:4978 [44] that represents locations using three orthogonal axes. This makes the AIS position compatible to our camera model.

With the aforementioned information from AIS we create a right handed object coordinate system v for each vessel in our three dimensional world space, representing the vessels position and orientation in it. The axis that points forward is \mathbf{x}_v . It lies on the tangential plane of the Earth at the point of the AIS antenna. We assumed roll and pitch to be zero, since vessels operate close to upright pose. Thus its direction is determined solely by the heading of the vessel. Likewise, \mathbf{y}_v is the orthogonal axis, that points to the vessels port side. \mathbf{z}_v is the "up" vector, that is the tangential plane's normal. All axes converge at the point determined by the AIS antenna location. The vectors used as the object system axes are normalised to a metre length. The origin and orientation of v represent the pose of the vessel, based on AIS data.

Together with the vessel dimensions from the static AIS report, we define the corners of the water-level plane segment, 3D points in our world space, as follows:

$$\mathbf{c1}_{3d} = \mathbf{a}_{3d} + (A \cdot \mathbf{x}_v) + (C \cdot \mathbf{y}_v) \quad (5)$$

$$\mathbf{c2}_{3d} = \mathbf{a}_{3d} + (A \cdot \mathbf{x}_v) + (D \cdot (-\mathbf{y}_v)) \quad (6)$$

$$\mathbf{c3}_{3d} = \mathbf{a}_{3d} + (B \cdot (-\mathbf{x}_v)) + (D \cdot (-\mathbf{y}_v)) \quad (7)$$

$$\mathbf{c4}_{3d} = \mathbf{a}_{3d} + (B \cdot (-\mathbf{x}_v)) + (C \cdot \mathbf{y}_v) \quad (8)$$

where A is the distance to bow, B is to stern, C is the distance to port and D is the distance to starboard from the AIS antenna location \mathbf{a}_{3d} . (see blue points in Fig. 3). Having established the corners of the water-level plane segment using the vessel's dimensions and location, it is important to consider the update frequency of the AIS messages. At the moment

of image acquisition, the most recent AIS message from the corresponding vessel may be up to ten seconds old, resulting in outdated location information. We create a dead reckoning vector, \mathbf{dr} , to mitigate the temporal inaccuracy in vessel location data caused by the update frequency of AIS messages (see the red arrow in Fig. 3). By scaling the forward vector \mathbf{x}_v with the vessel's speed and the age of the AIS message at the time of image acquisition, we update the location of the water-level plane segment (see orange points in Fig. 3).

D. Matching AIS data with 2D detection results

At this stage, the vessels are detected using an object detection model and their AIS based location is projected onto the images as a water-level plane segment. However, we still need to compensate for the inaccuracies in AIS location data and derive the air draught information to create accurate 3D bounding boxes for the detected vessels. As the next step, we want to fuse the two data sources by first associating the 2D bounding box, BB_{pred} , with the water-level plane segment.

We formulate the task of matching AIS messages to detected vessels as a bipartite graph matching problem [45]. One set of nodes are the detection bounding boxes of our object detector, BB_{pred} . The other set of nodes is derived from the AIS information in image space WP_{ais} . These two sets of nodes are fully connected in the graph, each edge being assigned the result of a weight function described in Eq. (14), representing a matching cost. This allows tuning matching performance by adjusting the weight function.

The object prediction nodes contain the information about the 2D bounding box and the confidence score of the network. BB_{pred} is such a prediction, defined as

$$BB_{pred} = [x_1, y_1, x_2, y_2, \text{score}] \quad (9)$$

where (x_1, y_1) and (x_2, y_2) are the two corners spanning the bounding box and score is the detection confidence.

We project our set of water-level plane segment points from world space c_{3d} into image space c_{img} using the camera model determined via PnP. The water-level plane segment is projected onto the image space as a convex quadrilateral. For these four points c_{img} , we create the minimal enclosing rectangle, WP_{ais} . This is so it has the same shape as the rectangular object prediction:

$$WP_{ais} = [\min_x(c_{img}), \min_y(c_{img}), \max_x(c_{img}), \max_y(c_{img})] \quad (10)$$

where $\min_x(c_{img})$ is the minimal x-coordinate of all water-level plane segment corners in the collection c_{img} , and the other min/max functions are defined accordingly.

The matching cost is calculated based on the distance between the predicted 2D bounding box, BB_{pred} , and the water-level plane segment, WP_{ais} , as well as the difference in their widths. These measures are taken in image space. A correct match between WP_{ais} and BB_{pred} is expected to show spatial proximity, with the width of BB_{pred} being approximately proportional to the WP_{ais} .

With the width w and height h of the image, the edge weight θ is defined as:

$$\Delta cx = \frac{\left| \frac{x_1 + x_2}{2} - \frac{\min_x(c_{img}) + \max_x(c_{img})}{2} \right|}{w} \quad (11)$$

$$\Delta bottom = \frac{|y_2 - \max_y(c_{img})|}{h} \quad (12)$$

$$\Delta width = \frac{|(x_2 - x_1) - (\max_x(c_{img}) - \min_x(c_{img}))|}{w} \quad (13)$$

$$\theta(BB_{pred_i}, WP_{ais_j}) = \begin{cases} \frac{2\Delta cx + \Delta bottom + \Delta width}{\text{score}}, & \text{if vessel not on border} \\ \frac{2\Delta cx + \Delta bottom}{\text{score}}, & \text{if vessel on border.} \end{cases} \quad (14)$$

We compute the distance between BB_{pred} and WP_{ais} as the sum of the distance between the centres of their x -coordinates (Eq. (11)), and the distance between their lower edges along y axis (Eq. (12)). This special treatment is necessary because we cannot meaningfully compare the upper edge of the prediction bounding box with the water-level plane segment, as the latter AIS information source contains no vessel height. We assign greater weight to the centre factor, as tide-induced variations can introduce inaccuracies in the vertical placement of the projected AIS bounding box, which are not accounted for in the projection.

The difference in bounding box width (Eq. (13)) is only considered if the prediction bounding box does not lie on the image borders (Eq. (14)). When a prediction is on the image border, it indicates that the vessel is not fully visible. In such cases, comparing the width of the clipped prediction with the width of the non-clipped AIS projection would be misleading. The missing $\Delta width$ factor favours matches on the image border, due to lowering the weight θ . At the same time the Δcx component is likely higher in those cases, as BB_{pred} is constrained to the image size while WP_{ais} can protrude, leading to an increase in the x centre difference. These factors oppose each other, so that we cannot find evidence for this design choice degrading our matching performance.

The score acts as a scaling factor, favouring high-confidence predictions while still allowing lower-confidence predictions with better spatial compatibility to be matched.

The graph method efficiently matches 2D bounding box predictions from the object detection model with AIS-derived boxes by finding the minimum weight matching. Due to its fully connected nature, there will always be a match possible. To improve accuracy, we set a maximum weight threshold to filter out irrelevant matches. This refinement allows the system to return "no match" for significant spatial discrepancies, size differences, or low confidence scores, ensuring only the most reliable matches are considered.

E. Correcting AIS data using visual cues

At this stage we have, for a single vessel instance, a match of a 2D bounding box in image space and a corresponding

water-level plane segment derived from AIS data. These two can deviate spatially; visual cues can help reducing this spatial deviation. For the rotation we rely on the AIS data, but for the location, we can use the 2D bounding box in image space as a constraint for the position of the water-level plane segment. This allows us to correct both temporal and spatial-accuracy errors in AIS data. We refine the AIS-based location prior by applying a correction vector $\Delta \mathbf{v}_{3d}$ to all points of our water-level plane segment, yielding the bottom four corners of our final 3D bounding box:

$$\mathbf{b}_{i3d} = \mathbf{c}_{i3d} + \Delta \mathbf{v}_{3d}, \quad \text{for } i = 1, 2, 3, 4. \quad (15)$$

$\Delta \mathbf{v}_{3d}$ is determined with the help of our camera model (Eq. (4)):

Since the transformation between image space and real-world space has been estimated, the edges of the 2D bounding box in image space can be brought into the real world by reversing the perspective projection (Eq. (4)). Each edge of the bounding box is transformed into a plane representing a constraint, and all four planes converge at the camera's location in the real world, \mathbf{C} . This location is determined by the extrinsic camera matrix, a parameter determined by PnP:

$$\mathbf{C} = -{}^c\mathbf{R}_w^T {}^c\mathbf{t}_w \quad (16)$$

We wrap the projection reversal of the camera model (Eq. (4)) in a function named *pld* (projection line direction) so that

$$L(\lambda) = \mathbf{C} + \lambda \cdot \text{pld}(\mathbf{p}_{img}) \quad (17)$$

L is a line in world space on which all points are projected to the same pixel p_{img} and λ is the distance of a point in the line from the camera.

The correction vector, $\Delta \mathbf{v}_{3d}$, is determined with spatial constraints using three camera model based planes (α, β, γ) corresponding to left, right and bottom edges of the 2D bounding box. The four corners of the 2D bounding box in image space BB_{pred} are referred to as: $\mathbf{p}_1 = (x_1, y_1)$, $\mathbf{p}_2 = (x_1, y_2)$, $\mathbf{p}_3 = (x_2, y_1)$, $\mathbf{p}_4 = (x_2, y_2)$.

The plane α is established to be positioned such that, when viewed from the camera's perspective, the entire vessel lies to the right of it.

The plane α with its normal vector \mathbf{n}_α are defined as:

$$\mathbf{n}_\alpha = \mathbf{z}_v \times \text{pld}(\mathbf{p}_{2img}) \quad (18)$$

$$\alpha : \{ \mathbf{X} \mid (\mathbf{X} - \mathbf{C}) \cdot \mathbf{n}_\alpha = 0 \} \quad (19)$$

α is orthogonal to the water surface and the projection line of \mathbf{p}_{2img} lies in α .

For each corner $\mathbf{c}_{3d}^{(n)} \in c_{3d}$ of the water-level plane segment in world space we calculate the distance to the plane α .

$$d_\alpha(\mathbf{c}_{3d}^{(n)}) = \frac{(\mathbf{c}_{3d}^{(n)} - \mathbf{C}) \cdot \mathbf{n}_\alpha}{\|\mathbf{n}_\alpha\|} \quad (20)$$

In this calculation, the distance can be negative, depending on which "side" of the plane $\mathbf{c}_{3d}^{(n)}$ is.

Similarly, we define a plane, β , for the right edge and another plane, γ for the bottom edge. Then the related distance

measures $d_\beta(\mathbf{c}_{3d}^{(n)})$ and $d_\gamma(\mathbf{c}_{3d}^{(n)})$ are calculated for β and γ , respectively.

Each plane can yield a proposal for $\Delta\mathbf{v}_{3d}$ that makes the water-level plane segment compliant with its constraint. We define $\Delta\mathbf{v}_{3d}$ by averaging the correction proposals determined by the three planes. The goal is to shift the water-level plane segment in the space between the three planes (α, β, γ). The top case is the default one, using all correction planes, the other special cases exclude the correction factor of a plane if it protrudes the image border:

$$\Delta\mathbf{v}_{3d} = \begin{cases} d_\gamma^{(k)} \mathbf{n}_\gamma + \frac{d_\alpha^{(i)} \mathbf{n}_\alpha}{2} + \frac{d_\beta^{(j)} \mathbf{n}_\beta}{2}, & \text{if } BB_{pred} \text{ in image} \\ d_\gamma^{(k)} \mathbf{n}_\gamma + d_\alpha^{(i)} \mathbf{n}_\alpha, & \text{if } BB_{pred} \text{ protrudes right,} \\ d_\gamma^{(k)} \mathbf{n}_\gamma + d_\beta^{(j)} \mathbf{n}_\beta, & \text{if } BB_{pred} \text{ protrudes left,} \\ d_\gamma^{(k)} \mathbf{n}_\gamma, & \text{if } BB_{pred} \text{ protrudes both sides.} \end{cases} \quad (21)$$

Correction in the image's depth is always applied via γ , side-wise correction is applied conditionally. In the first case, an average of the α and β corrections is applied when the object prediction bounding box does not touch the image edges. The other cases ignore the correction planes proposal if the bounding box edge they are derived from is caused by the image border.

F. Creating the 3D bounding box

Given the spatially corrected water-level plane segment, we can now complete the 3D bounding box, b_{3d} , that fully encompasses the vessel in 3D space. To substitute the lack of air draught information in the AIS data, we calculate an estimated height of the vessel, h_v , by shifting the water-level plane segment, \mathbf{c}_{3d} after correction, upwards, along the water surface's normal vector with $\Delta\mathbf{h}_{3d} = h_v \cdot \mathbf{z}_v$, aligning it with the top edge of the 2D bounding box.

We create a forth restriction plane δ using the upper edge of the 2D bounding box:

$$\mathbf{n}_\delta = \text{pld}(\mathbf{p1}_{\text{img}}) \times \text{pld}(\mathbf{p3}_{\text{img}}) \quad (22)$$

$$\delta : \{\mathbf{X} \mid (\mathbf{X} - \mathbf{C}) \cdot \mathbf{n}_\delta = 0\} \quad (23)$$

The distance function is defined similar to Eq. (20), but taking the correction vector into account:

$$d_\delta(\mathbf{c}_{3d}^{(n)}) = \frac{(\mathbf{c}_{3d}^{(n)} + \Delta\mathbf{v}_{3d} - \mathbf{C}) \cdot \mathbf{n}_\delta}{\|\mathbf{n}_\delta\|} \quad (24)$$

where $d_\delta^{(l)}$ is the distance to move our water-level plane segment upwards, until it touches the restriction plane γ . We thus set $h = d_\delta^{(l)}$.

We complete the 3D bounding box creating the top four corners by translating the corrected water-level plane segment \mathbf{c}_{3d} with the offset vector $\Delta\mathbf{h}_{3d}$ as follows:

$$\mathbf{b}_{i3d} = \mathbf{c}_{(i-4)3d} + \Delta\mathbf{v}_{3d} + \Delta\mathbf{h}_{3d}, \quad \text{for } i = 5, 6, 7, 8. \quad (25)$$

The bounding box created this way now spans the vessel in 3D space. We can calculate the vessel's centroid by averaging the corners, and the vessel's rotation is given by its object axes $\mathbf{x}_v, \mathbf{y}_v, \mathbf{z}_v$. Sample images with 6D pose annotations are visualised in Fig. 4.

IV. BOATS ON NORDELBE KEHRWIEDER DATASET

The BONK-Pose dataset we publish consists of 3753 images featuring a total of 3829 vessels, each annotated with their respective pose. The annotations include the vessels 3D centroid, its 3D dimension and rotation in 3D space. These 6D pose annotations are created by our automatic approach based on fusing the vessels' dimensions, heading and location from AIS messages with visual cues.

We initially collected 4176 monocular RGB images around the River Elbe, and relevant AIS messages. Applying our approach, we were not able to find AIS to vessel detection matches in all of them. We will look at the reasons for this in the Section V. A first comparison between vessel detections and the presence of vessel emitting AIS data already reveals discrepancies. The object detector often identifies more vessels in the images than are indicated by the AIS data. This mismatch may result from vessels not transmitting AIS, incomplete AIS data, or inaccuracies in the object detection model. We excluded those images from the final dataset, in which we were not able to find at least a single match.

The final dataset includes a diverse set of vessels: The occurrence distribution is skewed towards the public transport ferries and harbour tour vessels that regularly pass by the field of view. On the other hand, nearly 70 vessels are captured only once. Analysing the vessel sizes, we observed that most of them are relatively small, with lengths under 100 meters and widths less than five meters. However, the dataset also includes some larger vessels, providing a representation of different vessel types. Vessel locations are mostly centred in the middle of the field of view. The vessel centroids are 150 to 400 metres away from the camera position. Since the images are taken in an inland waterway, the distribution of the vessel rotations is less diverse, most vessels captured side-on.

We also created a manually annotated set of 1000 images with object detection ground truth. The object detection dataset has a intersection of images with the 6D pose estimation dataset, but is not a true subset. To evaluate the object detection models on vessels, we annotated vessels with 5 subclasses. Fig. 5 shows examples for all these classes. `ship` refers to a vessel cruising on the waterway, not touching the image edges. `ship_leaving_frame` is similar to `ship`, but it distinguishes vessels protruding beyond the image edge. `ship_moored` is used for vessels that are fully visible, but moored against the quay wall in the background and not moving. `ship_partial` is reserved for ship-like objects, which are mostly occluded, in the background, and not moving. This includes vessels being built in the dock in the background, the superstructure of cruise ships mooring in the far background, and generally parts that are known to be of vessels, but very difficult to identify. The `subvessel` class is used for cases in which there is a configuration of multiple independent



Fig. 4: Sample images from our dataset with pose annotations visualised.

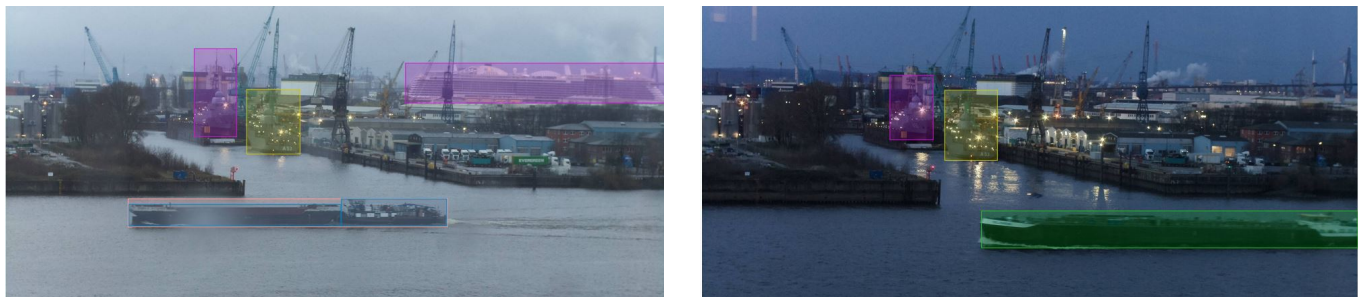


Fig. 5: Sample images from the dataset showing the 2D bounding box annotations with different sub-classes. Blue boxes highlight individual vessels in a barge-pusher setup, labelled as `subvessel`, while the entire setup is outlined in pink and labelled as `ship`. A cruise ship in the background or a ship in dry dock are marked with purple bounding boxes and labelled as `ship_partial`. The yellow box indicates a docked ship, labelled as `ship_moored`, and a green box shows a ship at the edge of the frame, labelled as `ship_leaving_frame`.

vessels travelling as a unit. For example, a pusher-barge unit is annotated as `ship` or `ship_leaving_frame` as whole and each part as a `subvessel`.

V. EVALUATION

A. Object detection results

To select an object detection model for our system, we evaluated multiple detectors on our manually created object detection dataset of 1000 images. We evaluated different network sizes (X, L, S) of YOLOX alongside YOLOv3, as it is the basis for YOLOX. Furthermore we evaluate DETection TRansformer (DETR) [46], its evolution Deformable DETR [47], and Cascade R-CNN with ResNet50 as backbone.

We will showcase results from two configurations, despite our annotation granularity allowing for more permutations. The first configuration involves using the classes `ship`, `ship_leaving_frame` and `subvessel` and the second

configuration includes all of our sub-categories for vessels. Since the models we compare are pretrained on the MS COCO dataset, we compare these custom labels to the `boat` class.

We expect AIS messages for the three classes in the first configuration, as these vessels are moving, making them relevant for our system. This configuration allows us to evaluate networks especially for our use-case. Correspondingly, `ship_moored` and `ship_partial` are not relevant for our approach, as we expect no AIS data to be available for them. By including all classes in the second configuration, we provide a general overview for the ship detection performance of the object detectors. Table I shows the performance of the detection models.

The results show that the combination of sub-classes `ship`, `ship_leaving_frame`, and `subvessel`, the relevant ones to our work, yields higher precision and recall than the one including all annotations. This suggests that

Ground truth	Metric	YOLOX-X	YOLOX-L	YOLOX-S	YOLOv3	DETR	Def. DETR	Def. DETR 2-Stage	Cascade R-CNN r50
Vessels relevant for our use case (S, SLF, SV)	mAP@.5:.95	0.626	0.603	0.542	0.379	0.451	0.510	0.585	0.511
	mAP@.5	0.805	0.794	0.764	0.659	0.696	0.737	0.775	0.725
	AR@100	0.756	0.746	0.698	0.549	0.645	0.703	0.761	0.680
All vessel like objects (S, SLF, SM, SP, SV)	mAP@.5:.95	0.398	0.363	0.277	0.232	0.278	0.337	0.372	0.309
	mAP@.5	0.588	0.550	0.457	0.476	0.513	0.562	0.571	0.527
	AR@100	0.514	0.473	0.429	0.332	0.398	0.447	0.531	0.427

TABLE I: mAP and AR of various detectors on our ship detection dataset with 1000 images. The sub-class names are shortened for a better presentation. S: ship, SLF: ship_leaving_frame, SV: subvessel, SM: ship_moored, SP: ship_partial. YOLOX-X and the two-stage deformable DETR are the best performing models from the pool we evaluated. Since YOLOX-X was faster in inference by a factor of 2-3 on our hardware, we ended up choosing it over the DETR based one. The table also shows that the vessels relevant for our approach are easier to detect than the vessels in the background.

ship_moored and ship_partial are harder to detect, as these vessels are often near quay walls and in front of a cluttered background. Especially ship_partial includes many objects such as hulls not in the water or only the superstructures of cruise ships, features that differ significantly in appearance from a hull in water.

For comparing our results with existing research, we also used a model that was fine-tuned on a similar dataset [11]. According to the results in [11], YOLOv5 achieved 0.332 mAP@0.5 without fine-tuning on their dataset. After fine-tuning on their dataset, the model’s performance improved significantly to 0.951 mAP@0.5. However, on our dataset, the YOLOv5 model fine-tuned on their dataset performed similar to the generalised YOLOX-S, with mAP@0.5 of 0.455 considering the configuration with all sub-classes. This shows that if we fine-tune a YOLOX-X model on our dataset, it may increase the performance on our dataset, but its transferability to other datasets will still be a question, especially as our scene is broadly static.

Therefore, to prove that our model can work with ”off-the-shelf” models, we select the YOLOX-X model pretrained on MS COCO as the object detector we deploy to verify our approach. This model achieves 0.80 mAP@0.5 on relevant sub-classes, and sufficiently supports the proposed technique’s performance. Moreover, the following section demonstrates that the object detection model does not significantly limit the performance.

B. Projection error of georeferenced data into image space

We evaluate the projection quality of the different projection methods via the average reprojection error of the annotated keypoints. We project all used world space keypoints into image space, then calculate the Euclidean distance between the transformed keypoints and the corresponding image keypoints. The camera was intermittently moved during data collection, leading to slightly changed viewports. For each transformation method, we calculate the average reprojection error of all keypoint correspondences over all viewports.

In Table II, we compare the average projection error over our three projection methods. The PnP method demonstrates a clear superiority, yielding a projection error that is one-fifth of the homography approaches. The differences between the two homography approaches are not significant. The PCA-based 2D projection plane improves the projection slightly compared to the water-surface-based projection plane. The higher error

Transformation	MAE	Error width %	Error height %
Perspective n-point (PnP)	12.22	0.48	0.64
Homography, Water surface	61.88	2.42	3.22
Homography, PCA	59.96	2.34	3.12
Homography in [11]	22.65	1.67	2.95

TABLE II: Resulting average projection errors for all transformation methods compared with [11]. The results are displayed as the mean absolute error (MAE) in pixels, the absolute error relative to the image width, and the absolute error relative to the image height.

in the homography approaches can be explained by the loss of one dimension of information. Many of the keypoints differ in height, and as the camera views the surface plane at a relatively flat angle, these height differences have a significant impact on the reprojection error. The PCA approach performs marginally better as it is designed to minimise the information loss caused by discarding the height dimension. Nonetheless, the inability to represent the height information makes it significantly worse than the PnP approach.

Table II also compares our results to those from [11], where they used homography for registering the image in the real world. Our PnP approach outperforms the homography-based approach in [11]. The performance of homography error relative to image size is slightly worse in our case. This discrepancy could be due to variations in the distribution of keypoints along the world axes. Selecting 3D keypoints that are near a plane, results in minimal information loss for homography. Conversely, if the keypoints are spread out across all three dimensions, the reprojection error tends to be larger.

Choosing real-world keypoints only on a plane enhances the average projection error metric, yet it does not address the inherent limitation of homography to project points not situated on the keypoint plane. Therefore, we demonstrate the superiority of employing the PnP method for converting between image and world space. Our approach requires PnP for the complete camera model and create 3D bounding boxes. However, related work on matching could also gain from the comprehensive three-dimensional mapping achievable with a perspective projection model, thereby improving the precision of projection when points are not coplanar.

C. Analysis of AIS and detection matching

To evaluate the performance of the matching algorithm, we analyse a randomly selected subset of 500 images from our dataset. In these 500 images, a total of 581 vessels are visible.

Association result	Quality/failure reason	Count	(%) over Grand Total	(%) in final dataset
Correct match	Good 3D bounding box	375	64.54	86.41
	OK 3D bounding box	33	5.68	7.60
	Bad 3D bounding box	2	0.34	0.46
	Total	410	70.56	94.47
Wrong match	Due to missing AIS data	9	1.55	2.07
	Due to false positive detection	2	0.34	0.46
	Due to cost function	9	1.55	2.07
	Subvessel and combined unit confusion	4	0.69	0.92
	Total	24	4.13	5.52
No match	Vessel not predicted	3	0.52	
	Vessel has no AIS	139	23.92	
	Vessel has neither prediction nor AIS	2	0.34	
	Has match and AIS, but cost was too high	3	0.52	
	Total	147	25.30	

TABLE III: Quality of Matching and 3D Bounding box creation of our system for 581 vessels across a sample of 500 images, categorised by match result (Correct match, Wrong match, No match). Subcategories show 3D bounding box quality or matching failure reasons. The final columns show the case distributions from two different perspectives: From the initial image set, over all vessels relevant for our system and from the final 6D pose estimation dataset resulting from our approach, where "No match" cases are excluded as they yield no annotations. This can be read as e.g.: From 100 vessel occurrences fed into our system, 71 were successfully associated with AIS messages; From 100 annotated vessels in our dataset, 94 annotations are based on a correct match.

Table III presents the distribution of results for matching vessel occurrences in the images with the AIS data, categorising them into correctly matched, incorrectly matched, or unmatched. For each image, we verified whether each vessel was successfully detected. We then checked the availability of AIS data for each detected vessel and manually assessed whether our matching algorithm correctly associated the 2D bounding boxes with their corresponding AIS data. Our matching algorithm achieves an overall accuracy of 70.56%, which is comparable to related work such as Lu et al.'s framework [7], obtaining 75.70% accuracy with DR, Huang et al.'s framework [22] achieving 74.3% accuracy on average, Qu et al.'s framework [9] with an overall accuracy of 81.42% and Gülsoylu et al.'s framework [11] with an average accuracy of 74.76%.

A correct match occurs when there is a predicted 2D bounding box around the vessel and it is correctly associated with the AIS data of the vessel in the bounding box. This is a prerequisite for creating a correct 3D bounding box for the vessel in the data fusion stage of our system. "Wrong match" occurs when the matching algorithm associates a vessel in a 2D bounding box with AIS data from a different vessel. This results in a 6D annotation that is based on incorrect AIS data, meaning that the vessel is annotated with e.g. wrong size or heading. A wrong match has the most detrimental effect on the quality of our dataset.

Wrong matches can occur when a false positive 2D bounding box gets matched with the AIS data of a nearby vessel, leading to a incorrect 3D bounding box creation for the actual vessel. Confusion between subvessels in multi-vessel units is another issue. If the AIS data describes only a part of the unit that is not visible, mismatched associations can occur, resulting in incorrect 6D pose annotations. Wrong matches may also stem from missing AIS data for the correct vessel. In such cases, the system matches detections with available AIS data from other vessels, leading to errors. Lastly, limitations in the cost function can lead to incorrect matches. Even when both detection and AIS data for the correct vessel are present, the

correct match can be forgone when the cost function selects another match with a lower cost.

"No match" refers to a vessel that is visible, but not detected or not associated with any AIS data by the bipartite graph matching. The most common reason for no match is the lack of AIS data. This can be caused by the vessel not transmitting AIS or the messages being missed by our capturing. Missing heading information of a vessel also makes it impossible to create an oriented water-level plane segment for the vessel, leading to the "No AIS" case. When the object detector fails to detect a visible vessel, this prevents a match from being made despite accurate AIS data. In some instances, neither a detection nor AIS messages exist for the vessel.

Overall, the availability of AIS data is the biggest limitation for correct matching, which can either prevent matching altogether or lead to inaccurate matches. In both cases, the correct match can not be created due to missing data, which then leads to no match being created or a wrong match being chosen instead. There is still improvement possible for the cost function and a better one could improve the fraction of correct matches in Table III further.

D. Analysis of AIS data correction quality

For the 581 vessels visible in the 500 images we sampled, our technique produced 410 matches, each leading to a 3D bounding box to be created. For each of those associations, we manually evaluated the quality of the resulting bounding box and categorised them into categories "Good", "OK", "Bad" and "Wrong match", as shown in Table III. This evaluation relied on manual effort.

"Good" annotations are those where the 3D bounding boxes precisely align with the actual pose of the visible vessel. These annotations accurately represent the vessel's position and orientation even in complex scenarios involving multiple vessels or partial occlusions. Examples for these are shown in Fig. 4. "OK" annotations are 3D bounding boxes that mostly fit the vessel but may have slight inaccuracies, such as an off-centre location or an skewed heading. An example is a vessel



Fig. 6: Examples of non "Good" annotations produced by our system. The left most one is an "OK" annotation, there is a mismatch between the heading in the AIS and in the actual rotation of the vessel visible. The middle one shows the object detector getting confused by the sailing boats masts and boat-spirit. This causes the 3D bounding box to be both offset to the left and much higher than it should be. It is a "Bad" bounding box. The right one shows a AIS based water-level plane segment being associated with a false positive detection, a "Wrong match" failure. This causes the 6D pose to be annotated in a region not containing a vessel.

manoeuvring in front of the camera. If the vessel is mid-turn, it may have a different heading in the image compared to the one transmitted in an outdated AIS message. This discrepancy causes the bounding box to be slightly rotated against the actual heading. This is shown in the left image in Fig. 6. "Bad" annotations are characterised by a significant deviation between the created 3D bounding box and the visible vessel, despite a correct association. For example, a sailing ship might be visible, but the object detector outputs a bounding box that includes background clutter as its masts. This causes the height inference to produce a bounding box that is much too big, an example shown in the middle of Fig. 6. For a "Wrong match", the 3D bounding box is always incorrect, often not fitting the dimensions, location, and heading of the visible vessel. A failure, resulting in a completely erroneous annotation, is shown in the right image in Fig. 6.

Since there is no ground truth for the height information, we cannot evaluate the output of our technique with commonly used 6D pose estimation metrics such as Average Distance-Symmetric (ADD-S) [48]. However, to put these quality categories into a quantitative frame of reference, we calculated the intersection over union (IoU) of a vessel's manually annotated 2D object detection bounding box and the minimal enclosing rectangle of the 3D bounding box created by our system. This IoU compares the rectangular 2D silhouette of our automatically created 3D bounding box in image space with the human annotated rectangular 2D vessel object ground truth. This measure is sensitive to spatial inaccuracies but less sensitive to rotational errors. Fig. 7 shows the distribution of our IoU measure categorised by the human assessment of the annotation quality. This calculation was performed on 245 images that are present in both the set of 1000 images annotated for object detection and in the final dataset of 3753 images produced by our approach.

We see that our quality assessment of the 3D bounding boxes, created by our system, correlates with the overlap between their projections in image space and the 2D object detection bounding boxes. We manually analysed the outliers that did not follow our expectation of "Good" annotations having a high IoU and "OK" and "Bad" ones having a lower

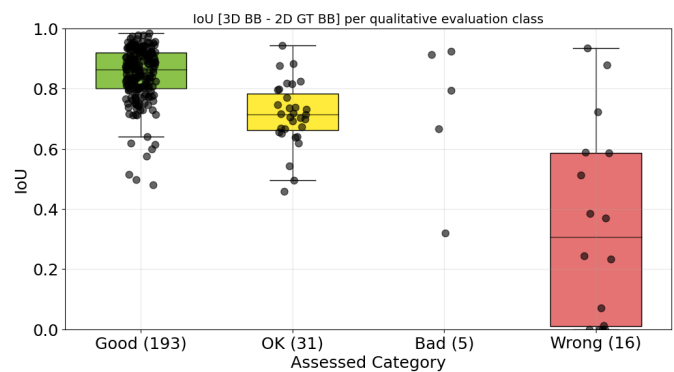


Fig. 7: IoU distribution of 2D bounding boxes and created 3D bounding boxes, separated by categories of manual quality evaluation.

IoU. We found that the samples with high IoU scores in the "OK" or "Bad" categories are not classified as "Good" due to heading errors. A 10° heading error has a low impact on the projection of the 3D bounding box and does not impede a high IoU score. In our quality assessment such a large heading error prevents classification as "Good". The lower IoU outliers in the "Good" category are due to differences in how antennas on vessels are handled. For example, if a 3D bounding box does not include the superstructure (e.g. antennas) fully due to mistakes in 2D bounding box prediction, the IoU is lower without necessarily making the pose not "Good".

Even though finding precise metrics to evaluate the performance of our system regarding the quality of the final 6D pose annotations is hard, without having objective 6D ground truth annotations already available, we have shown that there is a high percentage of good 6D pose estimation annotations created by our approach.

Missing AIS data is the most impactful factor reducing the share of correct and accurate annotations. Wrong matches are a significant source of incorrect 6D poses in the final dataset. Improvements in the cost function of the bipartite graph matching could increase the share of accurate annotations further, even as the current parametrisation is a local optimum devised in our experiments. The "OK" bounding boxes are caused by either a wrong 2D bounding box prediction or

inaccurate heading information from the AIS data. The former could be improved by fine-tuning the detector, the latter by a more sophisticated interpolation of the heading, by taking its rate of turn, and course into account.

VI. CONCLUSION

In this paper, we presented a novel technique to associate vessel detections on monocular 2D RGB images with AIS data for generating accurate 3D bounding boxes. Methods for coordinate transformation between GPS coordinates and image coordinates were compared, showing that a PnP-based approach achieves lower projection errors than previously used homography based ones. Multiple object detectors were benchmarked on a subset of our collected images, with YOLOX-X selected for its favourable speed-accuracy balance.

The matching problem was modelled as bipartite graph matching and the evaluation showed that the matching algorithm achieves an accuracy of 70.56%, which is comparable to related work [7], [9], [11]. The most common reason for incorrect matching is the lack of AIS data. Collecting Class B AIS data along with Class A could lead to better association.

Additionally, the paper introduces the BONK-Pose, a publicly available dataset comprising 3753 annotated images, which can be used for training and evaluating ship detection and 6D pose estimation networks. The quality of the final dataset is assessed manually and with the IoU of 2D bounding boxes and 3D bounding boxes in the image space. For vessels with successful matches, 6D poses were obtained by refining the AIS-based pose using visual cues derived from the monocular RGB images. The 6D pose annotation dataset created by our approach, without any manual posterior filtering, contains 86.4% correct annotations and 94.5% annotations of at least acceptable quality (see Table III).

Overall, the proposed technique demonstrates that fusing AIS data with object detections is a viable approach for creating accurate 6D pose annotations of vessels in maritime imagery. To further enhance the technique's performance, future work could focus on several improvements. Fine-tuning the object detection model can improve the detection quality.

A way to automate the registration of the viewport in the real world would be beneficial, to avoid the manual keypoint annotation that was necessary to solve the camera pose in the real world. Adapting this technique for a mobile setup with a camera and AIS antenna, would pave the way for a diverse image collection.

Finally, porting our approach to work on temporal image series could improve the matching accuracy, by combining an object tracker. Tracking the vessels would provide more information such as the movement direction and speed. These information can be auxiliary to the matching cost function.

REFERENCES

- [1] United States Coast Guard, "AIS Frequently Asked Questions," 2024, accessed: 2024-07-01. [Online]. Available: <https://navcen.uscg.gov/ais-frequently-asked-questions>
- [2] T. Emmens, C. Amrit, A. Abdi, and M. Ghosh, "The promises and perils of Automatic Identification System data," *Expert Systems with Applications*, vol. 178, p. 114975, 2021.
- [3] M.-C. Tsou, "Discovering knowledge from AIS database for application in VTS," *The Journal of Navigation*, vol. 63, no. 3, pp. 449–469, 2010.
- [4] "SAR ship detection and self-reporting data fusion based on traffic knowledge. author=Mazzarella, Fabio and Vespe, Michele and Santamaria, Carlos," *IEEE Geoscience and Remote Sensing Letters*, vol. 12, no. 8, pp. 1685–1689, 2015.
- [5] B. Murray and L. P. Perera, "An AIS-based deep learning framework for regional ship behavior prediction," *Reliability Engineering & System Safety*, vol. 215, p. 107819, 2021.
- [6] B. Zhang, J. Liu, R. W. Liu, and Y. Huang, "Deep-learning-empowered visual ship detection and tracking: Literature review and future direction," *Engineering Applications of Artificial Intelligence*, vol. 141, p. 109754, 2025.
- [7] Y. Lu, H. Ma, E. Smart, B. Vuksanovic, J. Chiverton, S. R. Prabhu, M. Glaister, E. Dunston, and C. Hancock, "Fusion of camera-based vessel detection and AIS for maritime surveillance," in *2021 26th International Conference on Automation and Computing (ICAC)*. IEEE, 2021, pp. 1–6.
- [8] E. Solano-Carrillo, B. Carrillo-Perez, T. Flenker, Y. Steiniger, and J. Stoppe, "Detection and geovisualization of abnormal vessel behavior from video," in *2021 IEEE International Intelligent Transportation Systems Conference (ITSC)*. IEEE, 2021, pp. 2193–2199.
- [9] J. Qu, Y. Guo, Y. Lu, F. Zhu, Y. Huan, and R. W. Liu, "Intelligent maritime surveillance framework driven by fusion of camera-based vessel detection and AIS data," in *2022 IEEE 25th International Conference on Intelligent Transportation Systems (ITSC)*. IEEE, 2022, pp. 2280–2285.
- [10] B. Carrillo-Perez, S. Barnes, and M. Stephan, "Ship segmentation and georeferencing from static oblique view images," *Sensors*, vol. 22, no. 7, p. 2713, 2022.
- [11] E. Gülsöylü, P. Koch, M. Yildiz, M. Constapel, and A. P. Kelm, "Image and AIS data fusion technique for maritime computer vision applications," in *2nd Workshop on Maritime Computer Vision (MaCVi), in Proceedings of the IEEE/CVF Winter Conference on Applications of Computer Vision*, 2024, pp. 859–868.
- [12] W. Gao, J. Liu, J. Zhi, and Z. Wu, "A Ship Tracking Method in Inland Waters Based on Fusion of Video and AIS Data," *IEEE Journal of Oceanic Engineering*, 2025.
- [13] G. Marullo, L. Tanzi, P. Piazzolla, and E. Vezzetti, "6D object position estimation from 2D images: A literature review," *Multimedia Tools and Applications*, vol. 82, no. 16, pp. 24 605–24 643, 2023.
- [14] H. Cao, L. Dirnberger, D. Bernardini, C. Piazza, and M. Caccamo, "6IMPOSE: Bridging the reality gap in 6D pose estimation for robotic grasping," *Frontiers in Robotics and AI*, vol. 10, p. 1176492, 2023.
- [15] A. Geiger, P. Lenz, and R. Urtasun, "Are we ready for autonomous driving? the kitti vision benchmark suite," in *2012 IEEE conference on computer vision and pattern recognition*. IEEE, 2012, pp. 3354–3361.
- [16] M. Reggiannini, E. Salerno, C. Bacciu, A. D'Errico, A. Lo Duca, A. Marchetti, M. Martinelli, C. Mercurio, A. Mistretta, M. Righi, *et al.*, "Remote sensing for maritime traffic understanding," *Remote Sensing*, vol. 16, no. 3, p. 557, 2024.
- [17] B. Hu, X. Liu, Q. Jing, H. Lyu, and Y. Yin, "Estimation of berthing state of maritime autonomous surface ships based on 3D LiDAR," *Ocean Engineering*, vol. 251, p. 111131, 2022.
- [18] E. Teixeira, B. Araujo, V. Costa, S. Mafra, and F. Figueiredo, "Literature Review on Ship Localization, Classification, and Detection Methods Based on Optical Sensors and Neural Networks," *Sensors*, vol. 22, no. 18, p. 6879, 2022.
- [19] H. Wang, Y. Yin, Q. Jing, Z. Cao, Z. Shao, and D. Guo, "Berthing assistance system for autonomous surface vehicles based on 3D LiDAR," *Ocean Engineering*, vol. 291, p. 116444, 2024.
- [20] V. Lepetit, F. Moreno-Noguer, and P. Fua, "EPnP: An accurate O(n) solution to the PnP problem," *International journal of computer vision*, vol. 81, no. 2, pp. 155–166, 2009.
- [21] G. Jocher, A. Chaurasia, A. Stoken, J. Borovec, NanoCode012, Y. Kwon, K. Michael, TaoXie, J. Fang, imyhxy, Lorna, Z. Yifu, C. Wong, A. V. D. Montes, Z. Wang, C. Fati, J. Nadar, Laughing, UnglvKitDe, V. Sonck, tkianai, yxNONG, P. Skalski, A. Hogan, D. Nair, M. Strobel, and M. Jain, "ultralytics/yolov5: v7.0 - yolov5 sota realtime instance segmentation," Nov. 2022. [Online]. Available: <https://doi.org/10.5281/zenodo.7347926>
- [22] Z. Huang, Q. Hu, Q. Mei, C. Yang, and Z. Wu, "Identity recognition on waterways: A novel ship information tracking method based on multimodal data," *The Journal of Navigation*, vol. 74, no. 6, pp. 1336–1352, 2021.
- [23] N. Wojke, A. Bewley, and D. Paulus, "Simple Online and Realtime Tracking with a Deep Association Metric," in *2017 IEEE International Conference on Image Processing (ICIP)*. IEEE, 2017, pp. 3645–3649.

- [24] X. Ma, W. Ouyang, A. Simonelli, and E. Ricci, "3d object detection from images for autonomous driving: a survey," *IEEE Transactions on Pattern Analysis and Machine Intelligence*, vol. 46, no. 5, pp. 3537–3556, 2023.
- [25] B. Kiefer, T. Höfer, and A. Zell, "Stable yaw estimation of boats from the viewpoint of UAVs and USVs," in *2023 European Conference on Mobile Robots (ECMR)*. IEEE, 2023, pp. 1–6.
- [26] A. Mousavian, D. Anguelov, J. Flynn, and J. Kosecka, "3d bounding box estimation using deep learning and geometry," in *Proceedings of the IEEE conference on Computer Vision and Pattern Recognition*, 2017, pp. 7074–7082.
- [27] T. Höfer, B. Kiefer, M. Messmer, and A. Zell, "HyperPosePDF Hypernetworks Predicting the Probability Distribution on $SO(3)$," in *Proceedings of the IEEE/CVF Winter Conference on Applications of Computer Vision*, 2023, pp. 2369–2379.
- [28] X. Song, P. Wang, D. Zhou, R. Zhu, C. Guan, Y. Dai, H. Su, H. Li, and R. Yang, "ApolloCar3D: A large 3D car instance understanding benchmark for autonomous driving," in *Proceedings of the IEEE/CVF conference on computer vision and pattern recognition*, 2019, pp. 5452–5462.
- [29] T.-Y. Lin, M. Maire, S. Belongie, J. Hays, P. Perona, D. Ramanan, P. Dollár, and C. L. Zitnick, "Microsoft coco: Common objects in context," in *Computer vision—ECCV 2014: 13th European conference, zurich, Switzerland, September 6–12, 2014, proceedings, part v 13*. Springer, 2014, pp. 740–755.
- [30] L. A. Varga, B. Kiefer, M. Messmer, and A. Zell, "SeaDronesSee: A maritime benchmark for detecting humans in open water," in *Proceedings of the IEEE/CVF winter conference on applications of computer vision*, 2022, pp. 2260–2270.
- [31] J. Qu, R. W. Liu, Y. Guo, Y. Lu, J. Su, and P. Li, "Improving maritime traffic surveillance in inland waterways using the robust fusion of AIS and visual data," *Ocean Engineering*, vol. 275, p. 114198, 2023.
- [32] T. Ferreira, A. Bernardino, and B. Damas, "6D UAV pose estimation for ship landing guidance," in *OCEANS 2021: San Diego–Porto*. IEEE, 2021, pp. 1–10.
- [33] "YOLOX: Exceeding yolo series in 2021."
- [34] J. Redmon, S. Divvala, R. Girshick, and A. Farhadi, "You only look once: Unified, real-time object detection," in *Proceedings of the IEEE conference on computer vision and pattern recognition*, 2016, pp. 779–788.
- [35] J. Redmon and A. Farhadi, "Yolov3: An incremental improvement," *arXiv preprint arXiv:1804.02767*, 2018.
- [36] T. Diwan, G. Anirudh, and J. V. Tembhurne, "Object detection using YOLO: Challenges, architectural successors, datasets and applications," *multimedia Tools and Applications*, vol. 82, no. 6, pp. 9243–9275, 2023.
- [37] L. Nie, C. Lin, K. Liao, M. Liu, and Y. Zhao, "A view-free image stitching network based on global homography," *Journal of Visual Communication and Image Representation*, vol. 73, p. 102950, 2020.
- [38] E. Vincent and R. Laganière, "Detecting planar homographies in an image pair," in *ISPA 2001. Proceedings of the 2nd International Symposium on Image and Signal Processing and Analysis. In conjunction with 23rd International Conference on Information Technology Interfaces (IEEE Cat)*. IEEE, 2001, pp. 182–187.
- [39] X. X. Lu, "A review of solutions for perspective-n-point problem in camera pose estimation," in *Journal of Physics: Conference Series*, vol. 1087, no. 5. IOP Publishing, 2018, p. 052009.
- [40] E. Marchand, H. Uchiyama, and F. Spindler, "Pose estimation for augmented reality: A hands-on survey," *IEEE transactions on visualization and computer graphics*, vol. 22, no. 12, pp. 2633–2651, 2015.
- [41] L. G. Shapiro and G. C. Stockman, "Computer Vision," *New Jersey, Prentice-Hall*, 2001.
- [42] A. Norris, "Automatic identification systems—the effects of class b on the use of class a systems," *The Journal of Navigation*, vol. 59, no. 2, pp. 335–347, 2006.
- [43] "EPSG:4979 – WGS 84," EPSG Geodetic Parameter Dataset, accessed: 2025-04-05. [Online]. Available: https://epsg.org/crs_4979/WGS-84.html
- [44] "EPSG:4978 – WGS 84," EPSG Geodetic Parameter Dataset, accessed: 2025-04-05. [Online]. Available: https://epsg.org/crs_4978/WGS-84.html
- [45] F. Serratosa, "Fast computation of bipartite graph matching," *Pattern Recognition Letters*, vol. 45, pp. 244–250, 2014.
- [46] N. Carion, F. Massa, G. Synnaeve, N. Usunier, A. Kirillov, and S. Zagoruyko, "End-to-end object detection with transformers," in *European conference on computer vision*. Springer, 2020, pp. 213–229.
- [47] X. Zhu, W. Su, L. Lu, B. Li, X. Wang, and J. Dai, "Deformable DETR: Deformable transformers for end-to-end object detection," *arXiv preprint arXiv:2010.04159*, 2020.
- [48] S. Hinterstoisser, V. Lepetit, S. Ilic, S. Holzer, G. Bradski, K. Konolige, and N. Navab, "Model based training, detection and pose estimation of texture-less 3D objects in heavily cluttered scenes," in *Asian conference on computer vision*. Springer, 2012, pp. 548–562.